Supplementary Information

High-speed panoramic light-sheet microscopy reveals global endodermal cell dynamics

Benjamin Schmid[1], Gopi Shah[1], Nico Scherf[2], Michael Weber[1], Konstantin Thierbach[2], Citlali Pérez Campos[1], Ingo Roeder[2], Pia Aanstad[3], Jan Huisken[1]*

[1]Max Planck Institute of Molecular Cell Biology and Genetics,
Pfotenhauerstr. 108,
01307 Dresden, Germany

[2]Institute for Medical Informatics and Biometry,
Medical School,
TU Dresden,
Fetscherstr. 74,
01307 Dresden, Germany

[3] Institute of Molecular Biology
and Center for Molecular Biosciences Innsbruck,
University of Innsbruck,
Technikerstr. 25,
A-6020 Innsbruck, Austria

* corresponding author: Jan Huisken, Huisken@mpi-cbg.de, +49-351-210-2487

Content

Supplementary figures

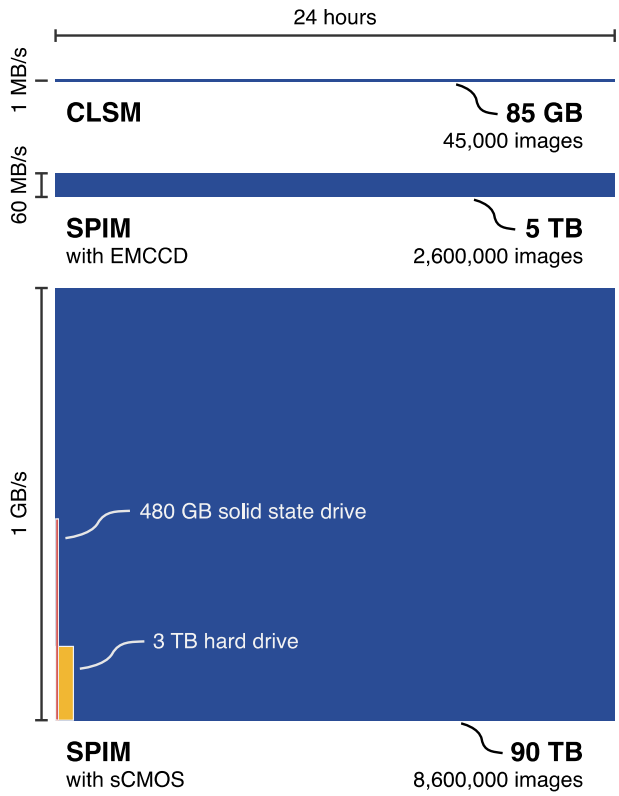

Supplementary Fig. S1: Data rates in confocal microscopy and SPIM

The data rates and the total amount of data for a 24-hour timelapse experiment are estimated for confocal microscopy and SPIM. While a confocal laser scanning microscope produces ca. 1MB/s, in SPIM an EMCCD camera generates ca. 60MB/s and an sCMOS camera ca. 1GB/s of image data. These rates result in ca. 1000 fold more data in SPIM as compared to a confocal microscope. This is far beyond the storage capacity and transfer rate for currently available hard drives (ca. 150MB/s; shown in yellow) and solid state drives (ca. 400MB/s; shown in red). While connecting multiple storage drives in a RAID configuration will increase the write speed and storage capacity, a major concern is to handle the huge amount of data for further processing and analysis. Therefore, extracting the useful information in real-time is a more efficient way and circumvents the intermediate storage of raw data while reducing the time required for post processing of the data.

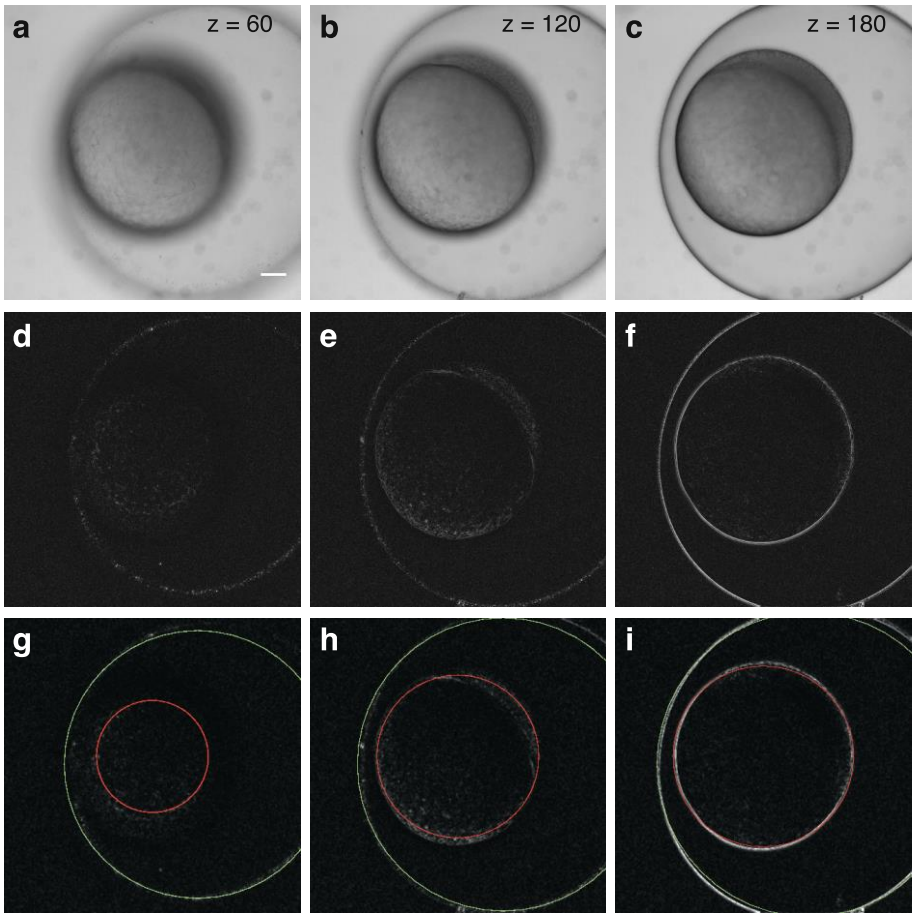

Supplementary Fig. S2: Sphere fitting to a transmission stack

(**a-c**) Transmission images of a zebrafish embryo showing different *z*-planes of the stack. (**d-f**) A Difference-of-Gaussian and a median filter are applied to highlight in-focus regions of the stack. (**g-i**) Fitting two spheres with a k-means like algorithm results in a larger sphere resembling the chorion and a smaller sphere resembling the zebrafish embryo. Scale bar 100µm.

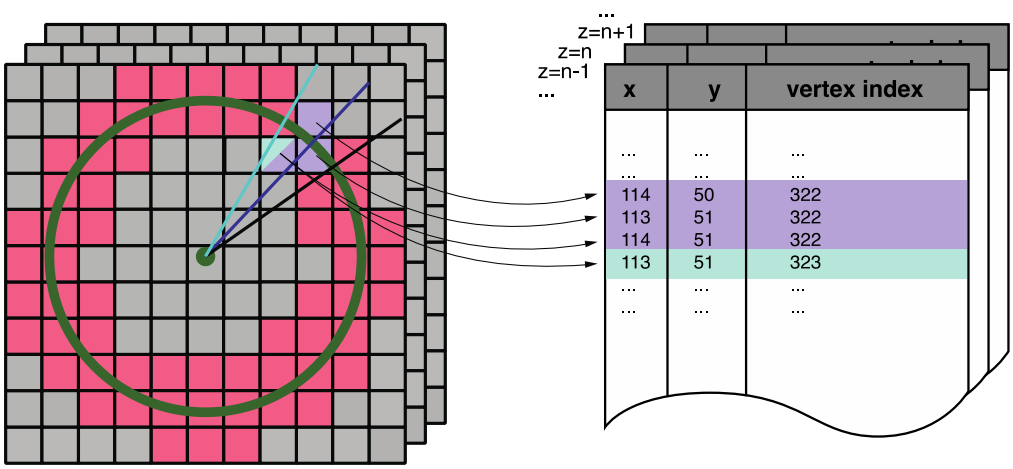

Supplementary Fig. S3: Lookup tables for real-time projection

Lookup tables were prepared to speed up real-time projection. The surface of the fitted sphere was evenly sampled, and rays were traced from the center to each vertex. Each ray intersects with a limited number of pixels, where only pixels within a specified shell around the sphere surface were taken into account (red area on the left side). The figure shows schematically the pixels of one such ray in purple. Each pixel may belong to more than one ray (cyan pixel). All pixels of a plane were collected in a lookup table, which stored the vertex index together with its coordinate. During real-time processing, the lookup-table of the currently imaged plane was recruited to process the pixels therein.

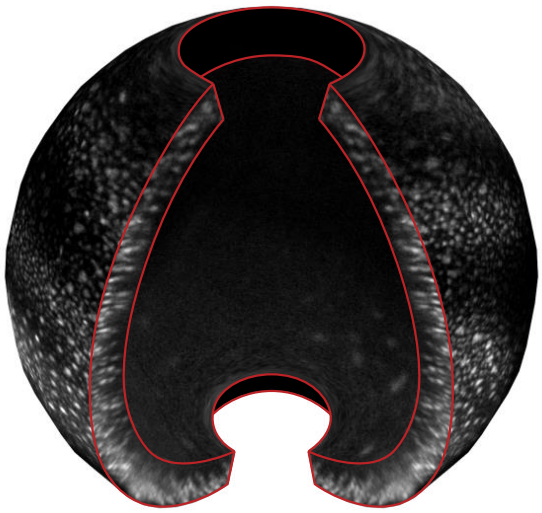

Supplementary Fig. S4: Multi-layered radial maximum intensity projection

Multi-layered radial maximum projection was applied to capture information from multiple cell layers in this embryo expressing H2A.F/z-GFP. The radius of the embryo shown is 333µm. The projection volume was split into 30 thin layers of 2µm each. In each of these layers, the maximum was determined separately.

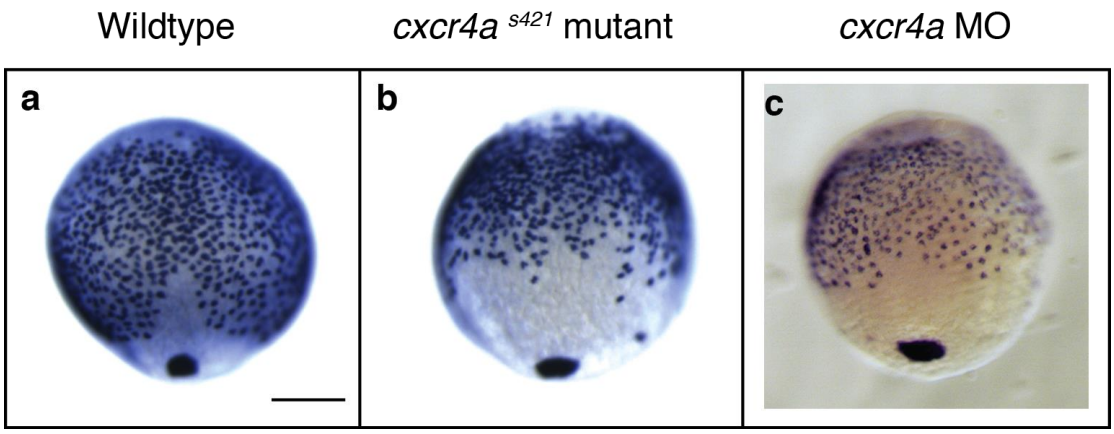

Supplementary Fig. S5: Endoderm cell distribution in *cxcr4a* mutant and morphant

Comparison of endoderm cell distribution between wild type, *cxcr4a* ^{s421} mutant and *cxcr4a* morphant at 10hpf, visualized by sox17 in situ hybridization. Scale bar: 200μm. **(a-c)**

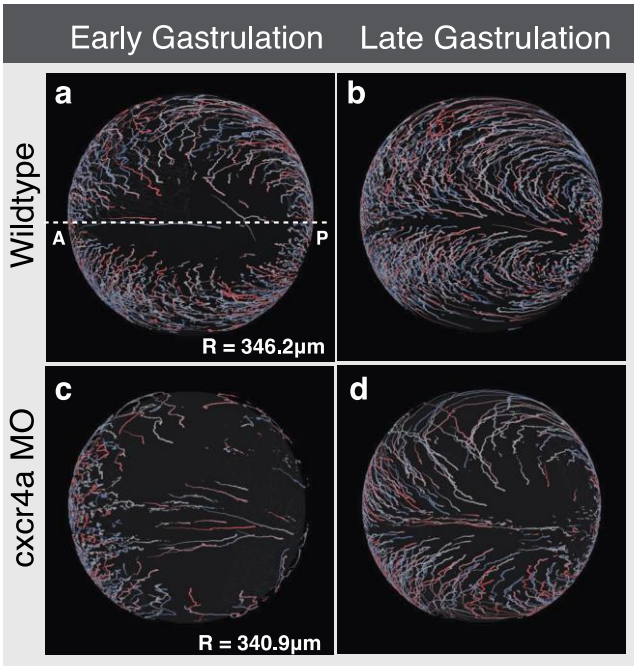

Supplementary Fig. S6: 3D rendering of cellular flows

3D rendering of cellular flows visualized on the spherical data **(a, b)** for wild type and **(c, d)** for cxcr4aMO for early and late gastrulation (compare Fig. 6).

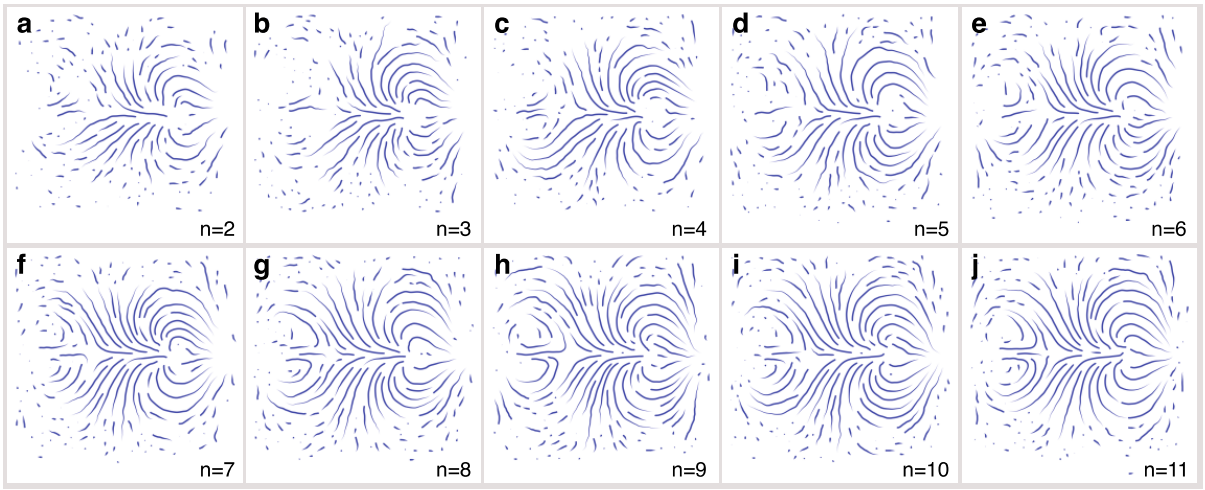

Supplementary Fig. S7: Average cellular flows

A montage of streamlines shown on Mercator projections. **(a-j)** Progression of averaged cell flows with increasing number of samples from n=2 to n=11.

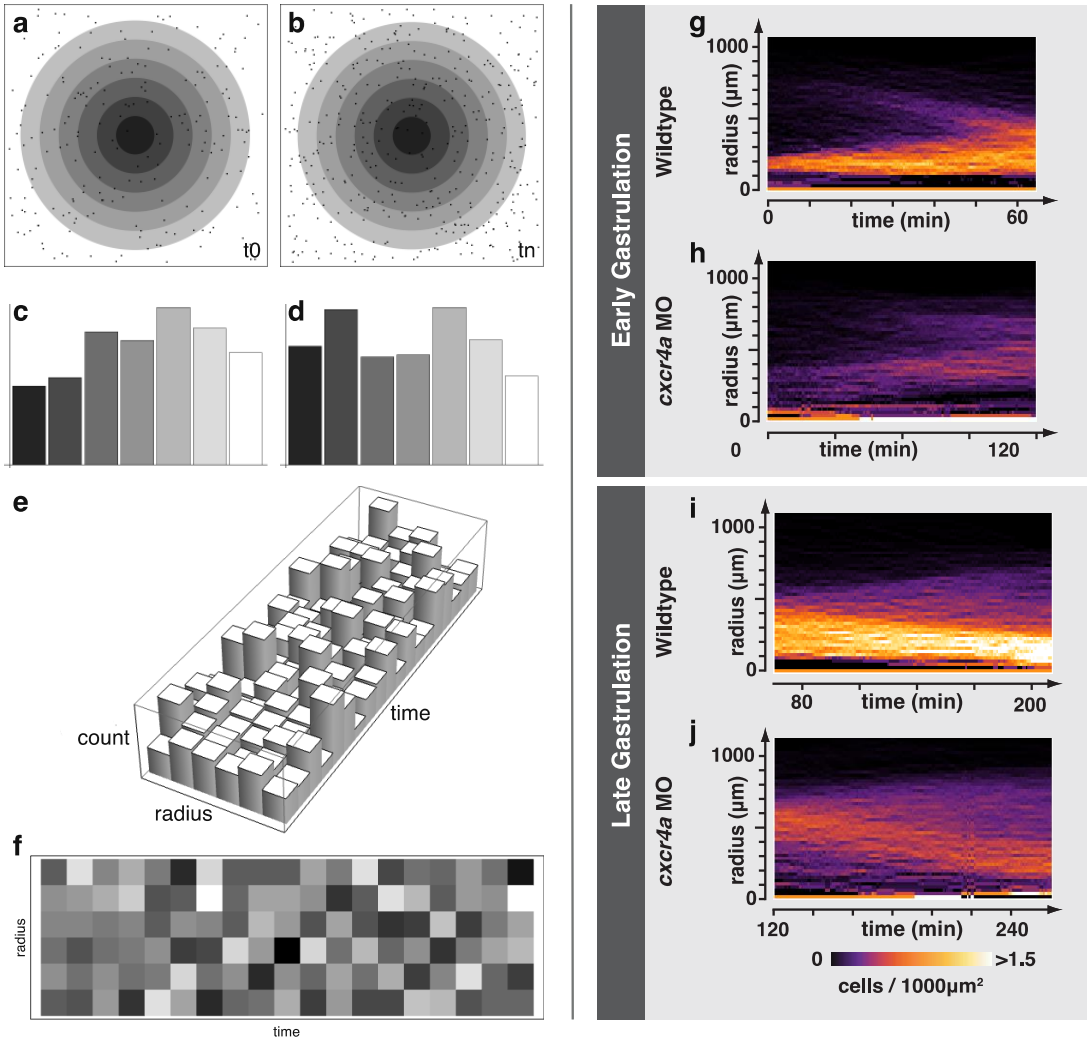

Supplementary Fig. S8: Schematic of the cell density kymograph

(**a**,**b**) Schematic of cell distribution (cells shown as black spots) around dorsal forerunner cells (DFCs, center). Cells were counted in annular regions with increasing radii (shaded regions) around DFCs for each time point. (**c**,**d**) Cell counts were normalized by area of respective annulus and data was represented as histograms. (**e**) Histograms for all time points were combined. (**f**) The final kymograph was obtained by taking the top view of concatenated histograms in **e**. **(g-j)** Kymographs corresponding to the density maps in Fig. 6.

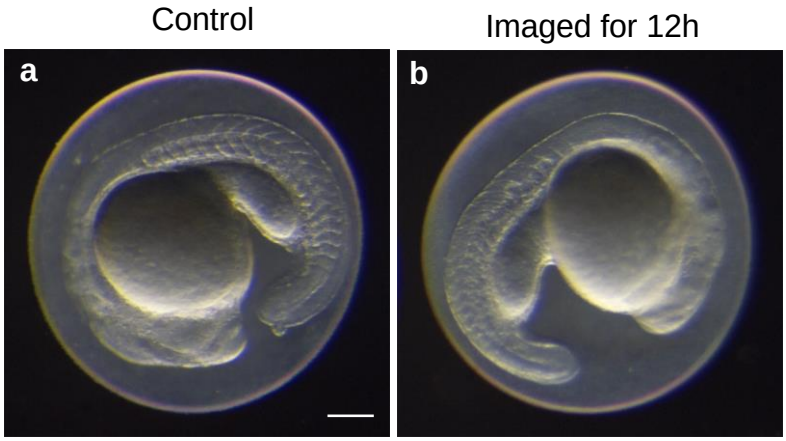

Supplementary Fig. S9: Control for photo-toxicity

Transmission image of wild-type embryos acquired at the end of a typical time-lapse experiment. Embryos were embedded in 1.5% agarose within the same FEP tube: **(a)** a control embryo that was not exposed to any light and **(b)** an embryo that was imaged for 12h. Scale bar 200µm.

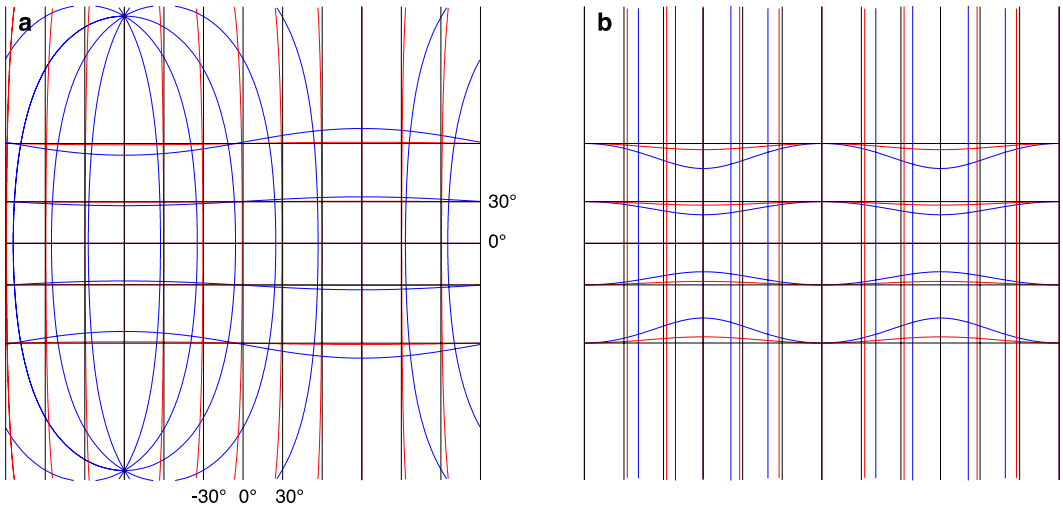

Supplementary Fig. S10: Distortions introduced by a non-fitting sphere in a Mercator projection

Meridians and parallels projected on a displaced sphere. (**a**) The original sphere was shifted by 1% (red) and 10% (blue) of the radius (**b**) The original sphere was stretched in the x-direction by 1% (red) and 10% (blue) of the radius.

Supplementary Methods

Microscope control. A custom LabVIEW (National Instruments) program was implemented to adjust stage positions, stack coordinates and various parameters for time-lapse acquisition. The speed of the *z*-motor was set to match the desired frame rate and the motor moved from the stack start position to the end. Other microscope parts were controlled via hardware triggers to ensure precise synchronization throughout the acquisition: The controller of the *z*-motor sent a digital trigger when it began to move. This signal was fed into a pulse generator, which alternately triggered the two lasers for left and right illumination. The same signal was also used to trigger the camera to acquire the desired number of images (given by the stack size). To account for the increase in fluorescence, the laser power was linearly reduced during the time-lapse.

Camera settings such as frame rate, exposure time, gain etc. were controlled with a custom Fiji plugin, which used the Java Native Interface (JNI) for calls of functions provided by the Andor SDK. The same plugin was used to read the images from the camera for further processing in Fiji.

Stage calibration. To calibrate the stage, green fluorescent beads were embedded in 1.5% agarose and imaged from seven different views: One stack was obtained at a reference position, three stacks after rotating the sample by 30°, 60° and 90° and three more stacks after translating the sample by 1µm in *x*-, *y*- and *z*-direction. A feature-based registration algorithm[16] was used to determine the rigid transformation aligning each of the six stacks to the reference stack. Every possible stage transformation could then be expressed as a combination of the six resulting transformation matrices. Stage calibration was performed once a day before the experiments were started.

Fitting a sphere to the transmission image. Before starting the timelapse acquisition, a single image stack was acquired using transmission light. Due to the limited depth of field, different parts of the embryo were in focus in different planes of the transmission stack. A difference-of-Gaussian approach[29] was used to filter efficiently for these in-focus regions:

$$I'(x,y,z) = |I(x,y,z) - G_\sigma(x,y) * I(x,y,z)| \qquad \text{(S1)}$$

where $I(x, y, z)$ denotes the intensity of the transmission image at pixel (x, y, z), $G_\sigma(x, y)$ is a 2D Gaussian kernel centered at (x, y) with a standard deviation σ and * denotes the convolution operator. Throughout our experiments we used σ =1.

Subsequently, a 3x3 median filter was applied to reduce noise. Two spheres were fitted to the resulting image stack by a custom algorithm motivated by the k-means algorithm. First, the image was roughly divided into foreground and background pixels by adjusting a global threshold. Foreground pixels usually

covered the surface of the embryo as well as the chorion. Two sphere models were then initialized, both centered at the image center and with estimated radii for the embryo and the chorion, 350µm and 550µm, respectively. An iterative, Expectation-Maximization-like algorithm was then executed, similar to the k-means algorithm: The expectation step assigned each foreground pixel to one of the sphere models, depending on its distance to the spheres' surface. The maximization step updated both sphere models from the assigned pixels using a least-squares fit. Both steps were repeated until convergence. The sphere model with the smaller radius resembled the embryo surface (Supplementary Fig. S2).

Image registration. Dense deformation fields between consecutive frames were obtained by applying a fast fluid image registration[26]. Briefly, a variational approach was used to obtain a mapping $\mathbf{u} = (u_1(\mathbf{x}), u_2(\mathbf{x}))$ from image I_n to I_{n+1}, minimizing an energy consisting of the sum of squared differences between the corresponding pixel values (over the whole image):

$$V(\mathbf{u}) = \iint \big(I_{n+1}(\mathbf{x}) - I_n(\mathbf{x} - \mathbf{u})\big)^2 \, \mathrm{d}\mathbf{x}, \tag{S2}$$

and a fluid regularization of the underlying field[26,30]:

$$T(\dot{\mathbf{u}}) = \rho \iint \sum_{i=1}^{2} \big(\Delta \dot{\mathbf{u}}_i(\mathbf{x}, t)\big)^2 \mathrm{d}\mathbf{x}. \tag{S3}$$

A minimizer of the combined energy $L(\dot{\mathbf{u}}, \mathbf{u}) = T(\dot{\mathbf{u}}) - V(\mathbf{u})$ was found by solving the corresponding Euler-Lagrange equation:

$$\rho \frac{d^2}{dt^2}(\Delta^2 \mathbf{u}) + \big(T(\mathbf{x}) - S(\mathbf{x} - \mathbf{u})\big)\nabla S(\mathbf{x} - \mathbf{u}) = 0. \tag{S4}$$

This partial differential equation was solved numerically to obtain the final displacement field[26,27]. Suitable boundary conditions for the Mercator projection were used (periodic for the x direction and reflecting for the y direction). All methods were implemented in C++.

Distortions introduced by a deformed sphere. Several circumstances may be responsible that the fitted sphere does not perfectly resemble the sample: (1) The surface of the embryo was not exactly spherical, (2) The embryo moved during the acquisition, (3) The embryo grew anisotropically during acquisition, (4) The sphere was not fitted correctly. To study the consequences we simulated a deformed sphere: We calculated the parallels and meridians of a sphere that is shifted or scaled in one direction. We found that a relative shift or anisotropic scale in one direction by one percent of the radius introduces minor distortions, which do not impair the interpretations of our data sets significantly, while a

displacement or scale by ten percent of the radius already introduces significant distortions (Supplementary Fig. S10).

In our endodermal experiments the embryo often moved vertically during the acquisition when embedded in glass capillaries. To detect such movements, we captured a transmission stack again at the end of the experiment and checked the position of the embryo. Experiments where the embryo moved more than one percent of its radius were discarded from further evaluation. Samples embedded in FEP tubes did not move during an experiment.

Cell tracking. Cells were tracked by propagating the detected cell masks with the obtained flow fields from the registration and subsequent consistency check[27]. Following steps were iterated throughout the sequence:

- The label image containing the detected cell masks from frame i were deformed by the displacement field between frame i and i+1.

- The deformed masks were checked for consistency by comparing the expected labeling of pixels from the registration with the labeling obtained from segmentation of frame i+1. The following cases were considered:

    1. If the label correspondences were one-to-one, the segmentation mask was used and the label was propagated accordingly.
    2. If several propagated labels were found within a segmented region (due to a visual overlap of cells), the separate masks from the registration were kept and the segmentation was discarded.
    3. In the case of cell divisions, two segmented masks overlap with one propagated mask. In this case, two new labels for the daughter cells were initialized and the segmentation masks were used for subsequent tracking.
    4. If a new object was detected and no propagated label was available (due to registration errors or erroneous segmentation in the previous frame), a new label was initialized.

The cell tracking script was implemented in Mathematica 8.0.

Supplementary References

29. Schindelin, J. Gaussian Stack Focuser: a fast and robust focusing technique. *in preparation*
30. Fischer, B. & Modersitzki, J. A unified approach to fast image registration and a new curvature based registration technique. *Linear Algebra Appl* **380,** 107–124 (2004).